

Submicrometer optical tomography by multiple-wavelength digital holographic microscopy

Frédéric Montfort, Tristan Colomb, Florian Charrière, Jonas Kühn, Pierre Marquet, Etienne Cuche, Sylvain Herminjard, and Christian Depeursinge

We present a method for submicrometer tomographic imaging using multiple wavelengths in digital holographic microscopy. This method is based on the recording, at different wavelengths equally separated in the k domain, in off-axis geometry, of the interference between a reference wave and an object wave reflected by a microscopic specimen and magnified by a microscope objective. A CCD camera records the holograms consecutively, which are then numerically reconstructed following the convolution formulation to obtain each corresponding complex object wavefront. Their relative phases are adjusted to be equal in a given plane of interest and the resulting complex wavefronts are summed. The result of this operation is a constructive addition of complex waves in the selected plane and destructive addition in the others. Tomography is thus obtained by the attenuation of the amplitude out of the plane of interest. Numerical variation of the plane of interest enables one to scan the object in depth. For the presented simulations and experiments, 20 wavelengths are used in the 480–700 nm range. The result is a sectioning of the object in slices 725 nm thick. © 2006 Optical Society of America

OCIS codes: 090.1760, 100.3010, 110.0180, 110.6960, 110.6880.

1. Introduction

The study of the internal structures of specimens has great importance in life and materials science. Thus different techniques of optical tomographic imaging have been developed to achieve the reconstruction of the optical properties of 3D specimens. The principle of so-called optical diffraction tomography (ODT) consists of recording the complex wave diffracted by a specimen while changing the \mathbf{k} vector of the illuminating wave. This way, the frequency domain of the specimen is scanned, allowing for the reconstruction of the scattering potential of the specimen in the spatial domain. The theoretical basis of ODT was established in the 1970s by Wolf,¹ Carter,² Dändliker and Weiss,³ and Fercher *et al.*⁴

In spite of the great application potential, few successful applications of the ODT techniques to microscopic imaging have been reported, certainly because the accurate recording of the complex diffracted waves may involve complicated implementations. Phase-shifting interferometry combined with varying the illumination direction was, for example, used by Lauer for the observation of bacteria and yeasts.⁵ Barty *et al.* obtained quantitative refractive index measurements on optical fibers, owing to their phase-retrieval algorithm based on three intensity measurements performed on different focus planes, combined with a rotation of the specimen relative to a fixed illumination beam.⁶ Recently, Charrière *et al.* demonstrated that digital holographic microscopy could successfully be applied to cell tomography,⁷ obtaining the first quantitative refractive index measurement with an ODT technique applied to a biological specimen.

Another way to perform ODT consists of changing the wavelength instead of changing the \mathbf{k} direction. In other words, the frequency domain and specifically the diameter of the Ewald is scanned by changing the wavelength. This technique, developed along the guidelines fixed by the diffraction tomography theorem (see also Refs. 1–4), may appear as rather complex and cumbersome in its practical application. In contrast, digital holography yields a particularly simple way to express indirectly the diffraction tomo-

F. Montfort (frederic.montfort@a3.epfl.ch), T. Colomb, F. Charrière (florian.charriere@a3.epfl.ch), J. Kühn, S. Herminjard, and C. Depeursinge are with the Institut d'Optique Appliquée, Ecole Polytechnique Fédérale de Lausanne, CH-1015 Lausanne, Switzerland. E. Cuche is with the Lycée Tec SA, PSE-A, CH-1005 Lausanne, Switzerland. P. Marquet is with the Département de Psychiatrie DP-CHUV, Centre de Neurosciences Psychiatriques, Site de Cery, 1008 Prilly-Lausanne, Switzerland.

Received 12 June 2006; revised 11 July 2006; accepted 11 July 2006; posted 13 July 2006 (Doc. ID 71850).

0003-6935/06/328209-09\$15.00/0

© 2006 Optical Society of America

graphy theorem: Remaining in the direct space, tomography of the object can be achieved by the superposition of reconstructed wavefronts from holograms taken at multiple wavelengths. This had been proposed several years ago by Marron and Schroeder⁸ and Marron and Gleichman,⁹ who called it holographic laser radar. They used an in-line holographic configuration in which the images are focused on the camera. The combination of several phase-shifted acquisitions allows the phase retrieval. Reference to a similar approach was also described by Arons and Dilworth¹⁰ as Fourier synthesis holography. More recently, the feasibility of section imaging by wavelength scanning digital holography was demonstrated by Kim^{11,12} and Yu and Kim^{13,14} on a macroscale. Dakoff *et al.*¹⁵ used the same method at the microscale but with an axial resolution of 11 μm .

In this paper, it is demonstrated that digital holographic microscopy (DHM), allowing us to reconstruct the complex wavefront of an object wave from a single recorded hologram,^{16,17} is a particularly well-suited technique to achieve multiwavelength tomography. Moreover, the digital optics developed by Colomb *et al.* and applied in this paper allows for the compensation of the phase aberrations,^{18,19} but also what is imperative is to reach the theoretical resolution limit of the method for chromatic aberrations (position and scale different for each wavelength wavefront reconstruction).²⁰ We demonstrate that DHM multiwavelength tomography enables, for the first time to our knowledge, the performance of tomographic imaging with an axial accuracy under the micrometer and a lateral resolution down to the diffraction limit without using a mechanical scan.

2. Digital Holography

A. Setup

The experimental setup is based on a classical Mach-Zehnder off-axis holographic interferometer (Fig. 1). The light source is generated by an argon-ion plasma laser (Coherent Innova 200) pumping a mode-locked Ti:sapphire laser system (Coherent Mira 900). The beam is then amplified by a regenerative amplifier (Coherent RegA 9000) and finally extended in a wavelength with a tunable optical parametric amplifier (OPA; Coherent OPA 9400). The beam coming from the OPA is split. On one side, the object beam O illuminates the sample through the microscope objective (MO; focal length of 18.4 mm, NA = 0.15, magnification of $\sim 10\times$) and the backscattered field, collected by the MO, interferes on the CCD with the reference beam R to produce a hologram. The irradiance at the specimen plane is of the order of hundredths of microwatts per square centimeter, slightly varying depending on the wavelength. In our case, the hologram is recorded in an off-axis geometry, meaning that a small angle θ is introduced between both waves. As the coherence length of the OPA beam is short ($\sim 60 \mu\text{m}$), the optical length of the reference beam is adjusted to the one for the object with a delay system (DS). Two more lenses are used: one is the

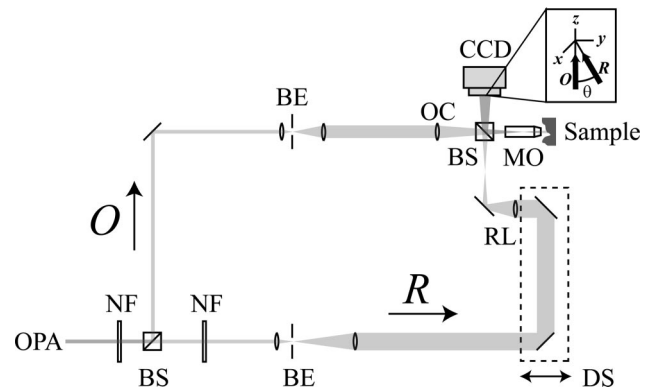


Fig. 1. Experimental setup. O , object arm; R , reference arm; OPA, adjustable wavelength laser; NF, neutral filter; BS, beam splitters; BE, beam expander; MO, microscope objective; OC, object beam condenser; RL, reference lens; CCD, charged-coupled device camera; DS, delay system.

object beam condenser (OC) that focuses the object beam at the back focal length of the microscope objective so it has a collimated beam illuminating the sample, and the second is the reference lens (RL) that curves the reference beam to match approximately the curvature introduced by the MO on the object beam in the CCD plane. This curvature matching is approximative and does not require an exact and delicate adjustment of the RL position because the residual curvature difference can be easily compensated for numerically as presented in the next subsection. We note that the image of the specimen through the MO is not focused on the CCD camera. The tomographic imaging will be computed from a sequence of 20 holograms recorded with 20 different wavelengths without moving any part of the setup, except the DS will compensate for dispersion between each wavelength and neutral filter to adjust the beam intensity.

B. Reconstruction Principle

The addition principle presented in Section 3 requires that the specimen size and position that appear in the reconstruction plane obtained from the different wavelengths must be identical. Ferraro *et al.*²¹ have demonstrated that a padding technique allows us to control the image size as a function of distance and wavelength within the single Fourier transform formulation of the numerical propagation in the Fresnel approximation. But the presented padding technique does not take into account the chromatic aberrations of the optics in the setup and especially those of the MO. Chromatic aberrations of the MO induce small differences in the magnification, the lateral position, and the focalization position of the specimen images. Therefore the convolution formulation is preferred with the advantage of keeping the pixel size constant at any reconstructed plane regardless of the reconstruction distance and enabling the use of numerical lenses to compensate for the chromatic aberrations as presented in Ref. 20.

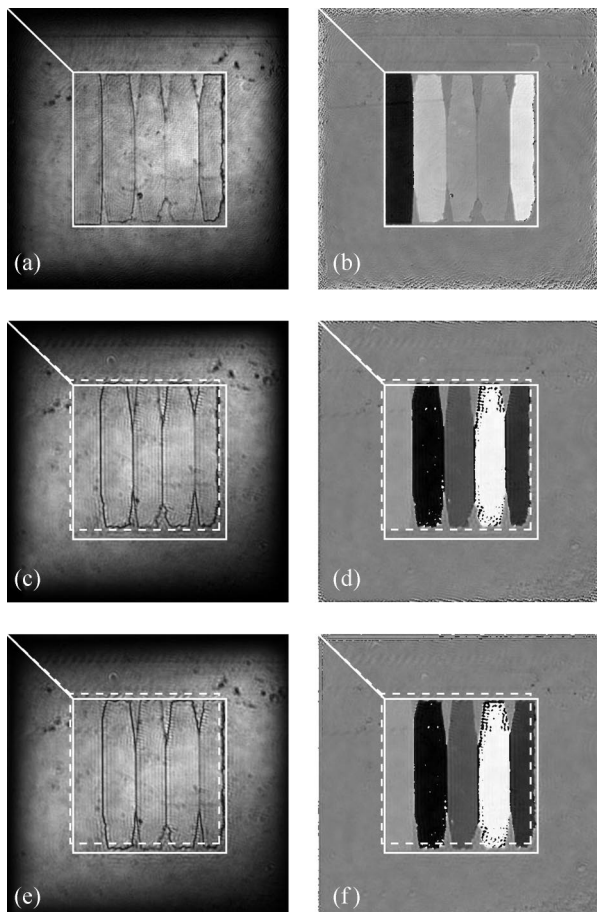


Fig. 2. Chromatic aberration compensation. The amplitude and the phase reconstructions are presented, respectively, on the left and on the right (the phase values between -180° and 180° are linearly distributed on the gray scaling). The wavelength and the reconstruction distances are (a), (b) $\lambda = 480$ nm, $d = 2.7$ cm and (c)–(f) $\lambda = 700$ nm, $d = -0.30$ cm. The white rectangles and lines define, respectively, the specimen size and position, (solid lines) for the reference defined at 480 nm and (dashed lines) for the reconstruction before the application of the numerical magnification and shift at 700 nm. (e), (f) Reconstructions by applying a magnification $M = 1.0038$ and a numerical shifting to achieve a perfect superposition of the reconstructed specimen for all the wavelengths.

The numerical reconstruction of the holograms is thus done in four steps. The first one consists of filtering in the hologram frequency domain the undesired diffracted images (zero order and conjugate image).²² The second one consists of compensating for the phase aberrations (tilt due to the off-axis geometry, curvature due to the MO not compensated for by the RL,²³ astigmatism, spherical aberration, etc.) by placing a numerical parametric lens in the hologram plane defined with a reference conjugated hologram¹⁹ or with an automatic fitting procedure.^{18,20} The third step is to propagate the corrected reconstructed object wave from the hologram plane to its focalization plane by adjusting the reconstruction distance [Figs. 2(a)–2(d)]. Finally, the sizes and the lateral positions of the specimen in the different reconstruction planes

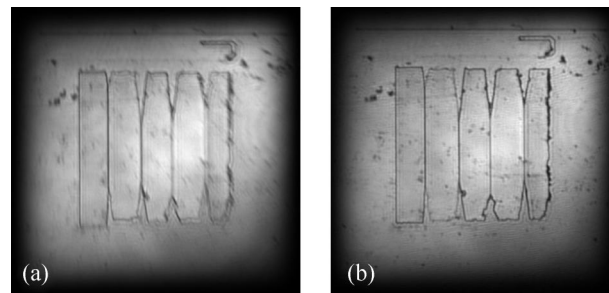


Fig. 3. Reconstructed mean amplitude from the 20 holograms recorded at different wavelengths (a) before and (b) after compensation of the chromatic aberrations.

are adjusted to be identical by the use of other numerical lenses as presented in Ref. 20 [Figs. 2(e) and 2(f)]. One should note that the aberration compensations, principally for the tilt, allow for the use of the convolution formulation of the Fresnel propagation (see Ref. 23 for the exact formulation of the convolution Kernel) without constraint in the reconstruction distance (small distances become possible without aliasing) giving no particular advantage to the so-called angular spectrum method as stated by Kim *et al.*²⁴

Figure 3 presents the average of the 20 amplitude images reconstructed from the 20 corresponding holograms recorded at different wavelengths: without [Fig. 3(a)] and with [Fig. 3(b)] the application of the numerical magnification and shifting procedure; Fig. 3(b) shows clearly that the procedure is essential for suppressing the blur because of the mismatch in size and position for the different wavefront reconstructions. In the case of a specimen composed of a constant step as presented here, this mismatch is responsible for a loss in resolution in the edges of the steps but has no influence on the axial accuracy in the central area of each step. This loss is difficult to describe analytically, as the tilt and scale factor due to chromatic aberration depends strongly on the experimental setup. The numerical correction here allows for the extension of the zone of maximal axial accuracy to the entire field of view, which is absolutely necessary for a reliable tomographic reconstruction in the case of a non-step-by-step constant specimen, in cellular imaging, for example.

3. Addition Principle

As already mentioned, the tomographic technique applied in the present work was first introduced by Marron and Schroeder⁸ and Marron and Gleishman⁹ and was later successfully applied to digital holography by Kim.^{11,12} The formalism used recalls the notations from Ref. 11 as well as some presentation aspects.

Let us assume that the different scattering centers in the specimen do not interfere with each other and that the scattering potential weakly depends on the wavelength. In this case, when the object is illuminated (IW in Fig. 4), the field diffracted by an object point P located at (x_0, y_0, z_0) and

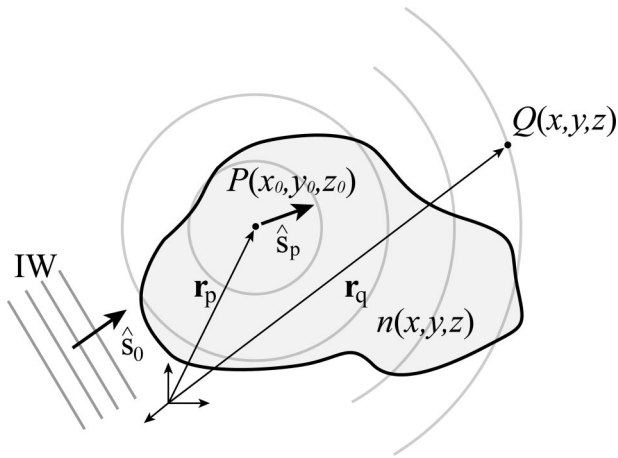


Fig. 4. Schematic of the scattering by a point P located at (x_0, y_0, z_0) and measured at an arbitrary point $Q = (x, y, z)$ within an object with refractive index distribution $n(x, y, z)$: IW is the illuminating wave, \hat{s}_0 is the incident wave direction, \hat{s}_p is the collection direction between P and Q .

$$\begin{aligned} \Psi(Q) &= \sum_{j=0}^{N-1} \Psi_j(Q) \\ &\propto \sum_{j=0}^{N-1} \int_V A(P) \exp(ik_j r_{PQ}) d^3 \mathbf{r}_{PQ} \\ &\propto \int_V A(P) \sum_{j=0}^{N-1} \exp(ik_j r_{PQ}) d^3 \mathbf{r}_{PQ}. \end{aligned} \quad (2)$$

Using the propriety $\sum_{j=0}^{N-1} r^j = (1 - r^N)/(1 - r)$ and writing $\bar{k} = (k_{\min} + k_{\max})/2$, this last equation can finally be written as

$$\Psi(Q) \propto \int_V A(P) \exp(i\bar{k} r_{PQ}) T(r_{PQ}) d^3 \mathbf{r}_{PQ}, \quad (3)$$

where $\exp(i\bar{k} r_{PQ})$ is a constant phase term. $T(r_{PQ})$ can be seen as an amplitude filter function with these extrema:

$$T(r_{PQ}) = \frac{\sin\left(\Delta k r_{PQ} \frac{N}{2}\right)}{\sin\left(\Delta k r_{PQ} \frac{1}{2}\right)} \text{ has } \begin{cases} \text{maxima for } r_{PQ} = p \frac{2\pi}{N\Delta k}, & p = qN \\ \text{minima for } r_{PQ} = p \frac{2\pi}{N\Delta k}, & p \neq qN \end{cases}, \quad (4)$$

measured at an arbitrary point $Q = (x, y, z)$ (Fig. 4) can be written as Huygens spherical wavelet proportional to $A(P) \exp(ik r_{PQ})$, where $r_{PQ} = n |\mathbf{r}_P - \mathbf{r}_Q|$ is the optical path length (OPL) between P and Q and n is the refractive index. The $1/r$ dependence of the amplitude may be neglected in the case of a microscopic object. For an extended 3D object, the field at Q is proportional to the above wave field integrated over all the points of the object in the volume V :

$$\Psi_j(Q) \propto \int_V A(P) \exp(ik r_{PQ}) d^3 \mathbf{r}_{PQ}. \quad (1)$$

Let us exploit the fact that a number N of copies of the electric field distribution can be generated by varying the wavelength (and thus the wavenumber k); let us take N \mathbf{k} vectors k_j lying within the range of $[k_{\min}, k_{\max}]$ regularly separated by Δ . We have

$$k_{\min} = \frac{2\pi}{\lambda_{\max}}, \quad k_{\max} = \frac{2\pi}{\lambda_{\min}}, \quad \Delta k = \frac{k_{\max} - k_{\min}}{N - 1}.$$

Assuming that the object illumination conditions are identical, the result of the superposition of the multiple electric fields at Q is

where p and q are integers.

If we consider an infinite wavelength range, then $T(r_{PQ})$ converges to a Dirac function:

$$\lim_{N \rightarrow \infty} \Psi(Q) \propto \int_V A(P) \exp(i\bar{k} r_{PQ}) \delta(\mathbf{r}_{PQ}) d^3 \mathbf{r}_{PQ} \propto A(Q). \quad (5)$$

In other words, the spatial contributions of the field diffracted from points other than Q are eliminated. In practice, if one uses a finite number N of wavelengths at regular intervals Δk , then the object image $A(P)$ repeats itself at axial distances $\Lambda = 2\pi/\Delta k$ with an axial resolution of $\delta = \Lambda/N$. By using appropriate values of Δk and N , Λ can be matched to the axial extent of the object and δ to the desired level of axial resolution. An example of this amplitude filter function is presented in Fig. 5.

Note that because the different complex fields required for tomography are acquired in the present work in a reflection geometry, the light travels back and forth in the medium. For two points defining a ray parallel to the optical axis, the measured optical path length r_{PQ} thus corresponds to twice the OPL between P and Q . The definition of r_{PQ} considering the reflection geometry is thus $r_{PQ} = 2n |\mathbf{r}_P - \mathbf{r}_Q|$. The effective axial resolution and axial extent have thus to be divided by a factor of 2. In the following text, the presented values of the OPL will be considered for the

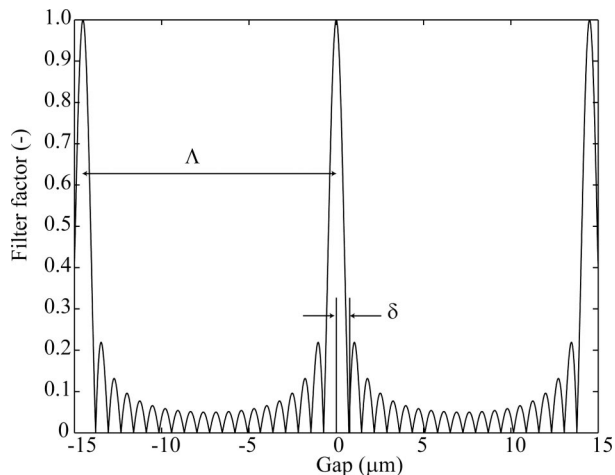


Fig. 5. Filter obtained by the sum of 20 k regularly separated wavelengths taken between 480 and 700 nm. Axial extent of $\Lambda = 14.5 \mu\text{m}$, axial resolution of $\delta = 725 \text{ nm}$.

reflection geometry and the reflective effective path lengths as already considered in Fig. 5.

4. Digital Holographic Microscopy Tomography

Several holograms of the object are taken at different wavelengths and each corresponding electric field distribution is reconstructed independently at its own wavelength and corrected for phase and chromatic aberrations as described above. The retrieved complex wavefronts Ψ_j correspond to the waves backscattered by the object. Note that the phase of each wavefront is defined up to a constant offset that is different for each wavelength. This floating phase introduces a random phase factor φ_j in Eq. (2):

$$\Psi(Q) = \sum_{j=0}^{N-1} \Psi_j(Q) \exp(i\varphi_j). \quad (6)$$

To obtain the sectioning effect thanks to the addition of complex fields, all the fields Ψ_j at the object point P must have the same phase. If not, the wavefronts will sum up in a random way, which prevents a constructive addition of the Ψ_j amplitudes.

Compared to previous works,^{11,12} we have implemented here the technique originally described by Marron and Schroeder⁸ and Marron and Gleichman⁹ in the direct space instead of the Fourier space. The handle of this floating phase is problematic; it takes advantage of the full numerical access to the reconstructed data. The method is based on the selection of a reference zone in the image (dashed rectangles in Fig. 6), which corresponds to a purely reflective area of the specimen, knowing therefore that all the illuminating wavefronts at different wavelengths have been reflected identically on that specific zone. A phase shift is then numerically introduced in each reconstructed wavefront to get the same phase on the selected reference zone (Fig. 6). This is performed by subtracting the mean phase value in the reference zone from the whole phase map in the image, fixing the phase to zero for every point in this zone. When

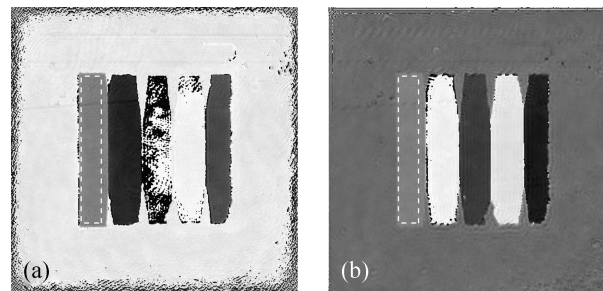


Fig. 6. Application of a phase shift to obtain the same phase on the selected reference zone defined by the dashed rectangle. The mean phase values computed in the same area defined in Figs. 2(b) and 2(f) are subtracted from the entire phase images of Figs. 2(b) and 2(f) and give, respectively, (a) and (b).

summed up, the Ψ_j will add constructively for that reference zone and every other point of the object having a similar phase defining a tomographic section of isophase surfaces.

Once the Ψ_j are referenced, tomographic sectioning can be performed in any further plane of interest a distance of ϵ in the OPL from the reference zone by adding a proper constant given by Eq. (7) to the phase of each wavefront. An OPL ϵ above or behind this zone involves a phase difference $\Delta\varphi$ depending on the wavelength λ_j :

$$\Delta\varphi_j = \frac{2\pi}{\lambda_j} \epsilon. \quad (7)$$

The reference area has thus to be selected only once to scan the whole specimen in depth. One should note that the presence of a reference zone in the field of view is mandatory for the proposed technique. In the case of a noisy or diffuse specimen, one should define a reference zone as large as possible to remove the random noise and keep only the average offset value of the area. If the entire field of view is strongly diffusive or composed of multiple layers contributing to the backscattered collected signal the described strategy cannot be directly applied.

5. Simulations and Experiments

Simulations and experiments have been conducted to demonstrate the validity of the method. Twenty holograms have been both simulated and recorded experimentally with regularly k -spaced wavelengths in the 480–700 nm range. The corresponding amplitude filter created by summing the given 20 wavefronts is the one presented in Fig. 5. Thus the resolution δ is given by the first zeros of the function and the axial extent Λ by distance between two maxima. With the used parameters, the axial resolution is 725 nm, and the axial extent is 14.5 μm .

A custom test target has been designed to estimate the resolution of this tomographic method and to see if the experimental tomographic filter corresponds to the above-presented filter function. First, simulations have been created with a digital version of the test target specimen (Fig. 7), defined as five steps

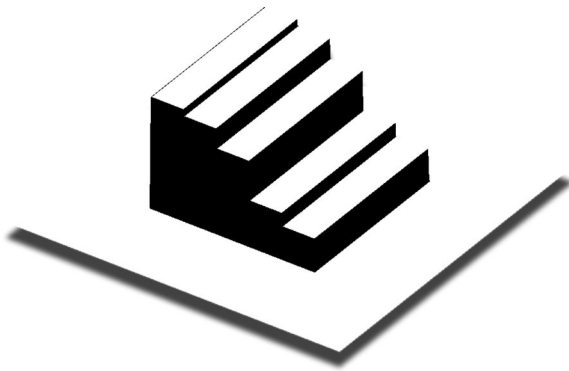


Fig. 7. Simulated target with steps of 375, 525, 975, 1200, and 1275 nm.

of 375, 525, 975, 1200, and 1275 nm heights, each 50×250 pixels large, in the center of a 512×512 pixel matrix. The wavefronts reflected by this specimen at all the different wavelengths are, respectively, calculated and propagated according to the Fresnel integral over a distance d (20 cm) to the hologram plane. Each wavefront is then superimposed to the corresponding reference wave, and the resultant intensities form the simulated holograms reconstructed as described above.

Second, experiments have been conducted using a homemade realization of the same test target built by structuring silicon oxide (SiO_2) layers on a silicon

wafer. The sample is $250 \mu\text{m}$ large with five steps of equal dimensions. Nevertheless, due to etching properties, the highest steps are no longer perfectly rectangular but have been attacked in the corners during manufacturing. A Plasmos SD2300 ellipsometer has been used to accurately verify that the height of all the steps corresponded to the designed values (errors below 2%). The wafer has finally been recovered with 10 nm chrome and 100 nm gold to ensure a total reflection on its surface.

6. Results

The results of the tomographies are shown in Fig. 8: The tomographies obtained with the simulated holograms are presented on top, and on the bottom those obtained with the experimental holograms are shown. The heights of the six reconstructed sections are those of the base [Figs. 8(b), 8(B)—0 nm] and the five steps of the specimen [Figs. 8(c), 8(C)—375, 8(d), 8(D)—525, 8(e), 8(E)—975, 8(f), 8(F)—1200, and 8(g), 8(G)—1275 nm]. Amplitude images, calculated as the average of all the reconstructed Ψ_j amplitudes, are shown in Figs. 8(a) and 8(A) for both the simulated and the experimental specimens. The presented tomographic sections clearly show the attenuation of the out-of-focus planes: They get darker as the distance to the plane of interest increases. Each step is distinct from the others due to the filter produced by the addition of the complex wavefronts. The steps that are separated

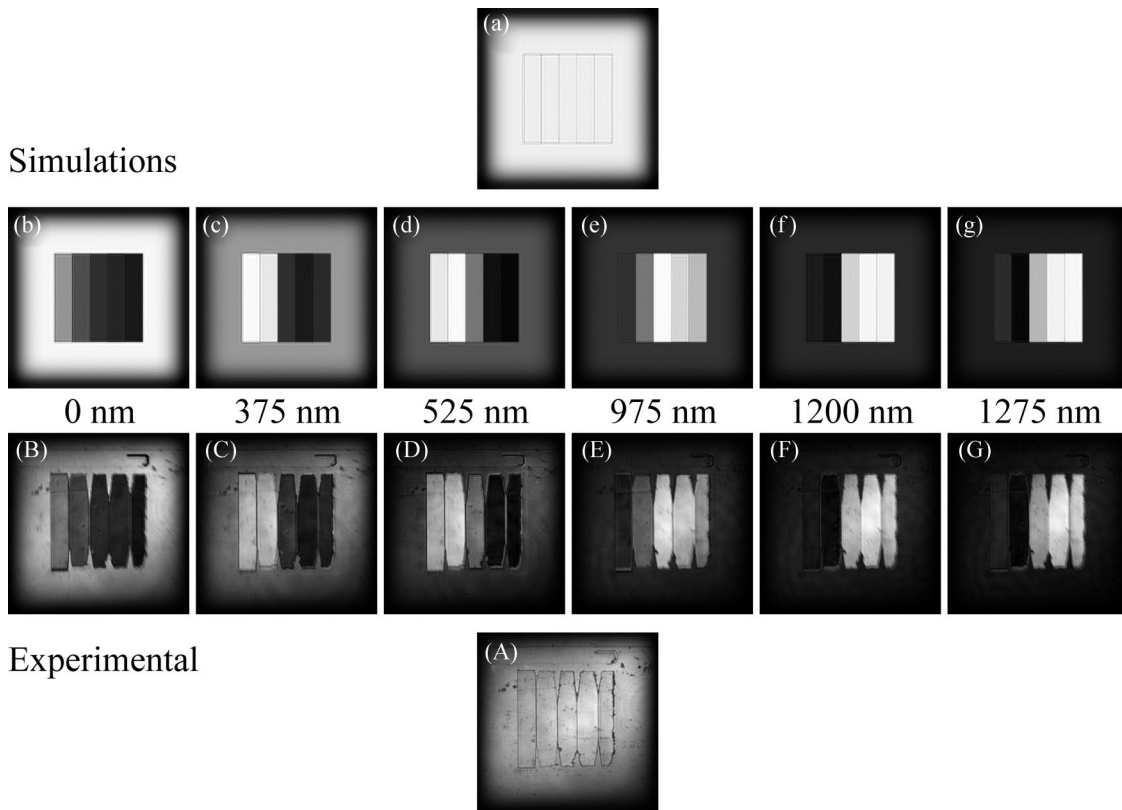


Fig. 8. Simulated (lower-case letters) and experimental (upper-case letters) results of six reconstructed sections at 0, 375, 525, 975, 1200, 1275 nm [(a), (b), (c), (d), (e), (f), respectively] as well as the specimen average amplitudes of the (a) simulated and (A) experimental targets.

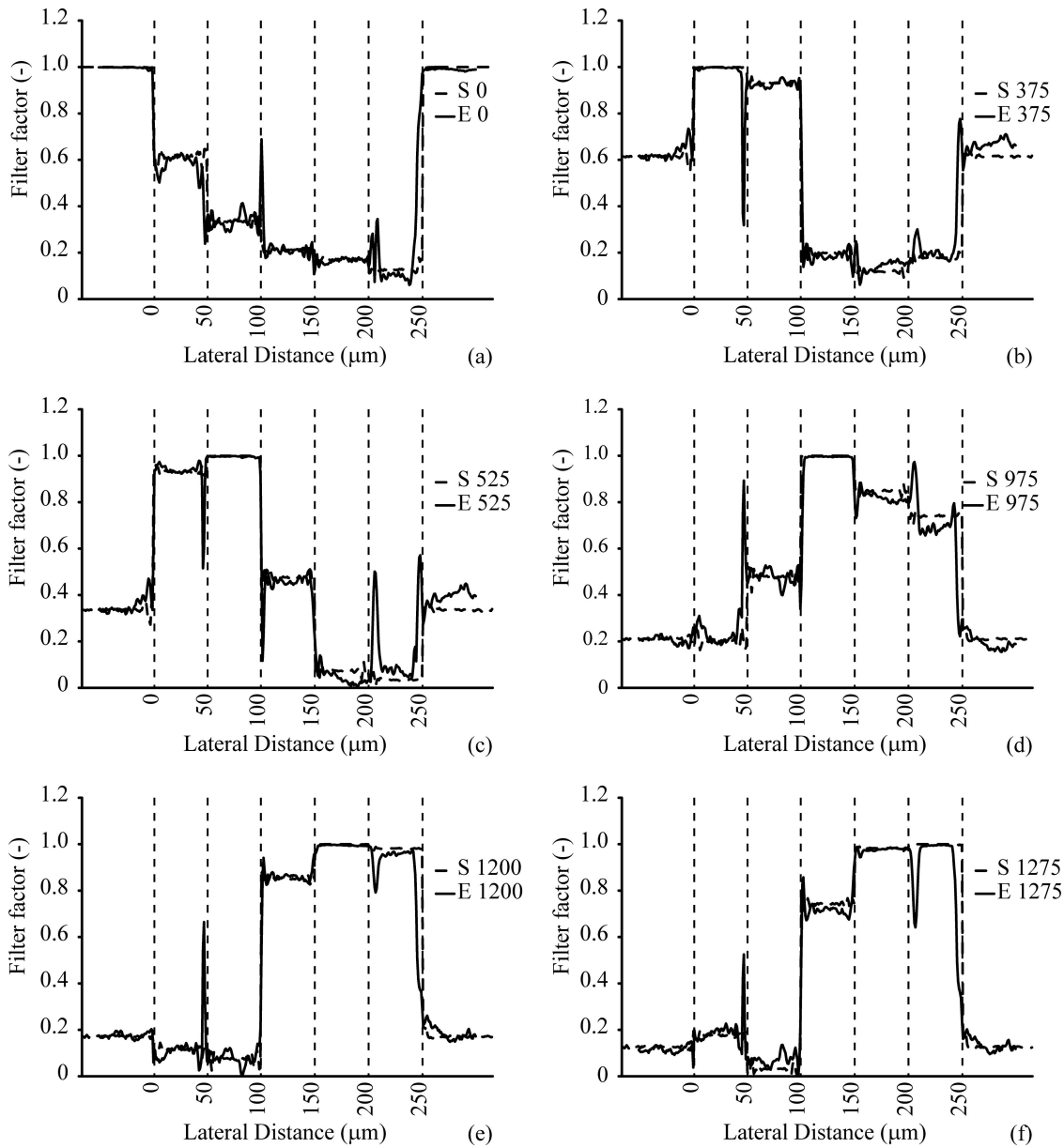


Fig. 9. Normalized intensity profiles $T(r_{PQ})$ for the 0, 375, 525, 975, 1200, 1275 nm planes of interest [(a), (b), (c), (d), (e), (f), respectively]. S denotes the results for the simulated specimen and E is for the experimental data.

from the step of interest within a gap smaller than the axial resolution are not clearly eliminated, owing to the insufficient attenuation of the filter. The best attenuation is obtained for a gap of 750 nm as shown in Figs. 8(d), 8(D) and 8(g), 8(G) between the second (525 nm) and the fifth (1275 nm) steps for negative [Figs. 8(d), 8(D)] or positive gaps [Figs. 8(g), 8(G)]. This corresponds to the theoretical predictions where the first total cancellation of the filter function is obtained at 725 nm. The 750 nm gap is clearly the nearest available gap; the theoretical resolution is verified in both simulated and experimental results.

These considerations can be quantitatively confirmed with the filter coefficient profiles defined by the division of the tomographic images by the amplitude image without tomography across the center of

the image. Figure 9 shows that for a coefficient equal to 1, the plane is unfiltered and corresponds to the plane of interest. The larger the gap from this reference plane, the lower the filter coefficient and the corresponding intensity.

The resolution of the tomography is also shown in Figs. 9(c) and 9(f) where the 750 nm gap is present. The 1275 nm step in Fig. 9(c) and the 525 nm one in Fig. 9(f) are nearly zero. Theoretically, the filter function value should be 0.033. The coefficients for the simulations are 0.033 and 0.044 for Figs. 9(c) and 9(f), respectively, and 0.088 and 0.132, respectively, for the experimental data.

The six sections in the tomography also enable us to retrieve the filter function curve as shown in Fig. 10. The curve is the theoretical prediction and the

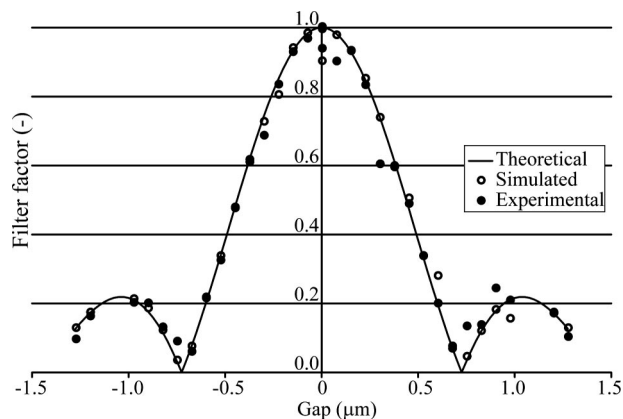


Fig. 10. Filter function curve $T(r_{PQ})$ with theoretical, simulated, and experimental points.

points represent the results of the tomographic process with white dots for the simulation and black ones for the experimental data. A section has been created at each step and at the base of the test target. For each of the six sections, the mean value of the filter function has been measured on each step and on the bottom (six mean values for each section). These values have been reported on the graph regarding the gap between the measured step height and the sectioning plane height (plane of interest). The slight imperfections in the reconstruction process, such as the adjustment of the reference wave parameters and the filtering of the zero order and the twin images, influence both the experimental results and the simulations, while the setup imperfections (lenses and beam splitters, for example) and the wavelengths' precision influence only the experimental data. Another error comes from the incertitude on the height of the experimental specimen that can reach up to 2%. The standard deviation with the theory is 2.6×10^{-2} for the simulation and 3.9×10^{-2} for the experimental results, demonstrating excellent agreement and consequently independently validating the reconstruction process as well as the experimental setup.

7. Conclusion

Submicrometer tomography can be performed on microscopic samples using DHM. Simulations and experiments validated the statement of the proposed method. Optical sectioning with a resolution of 725 nm has been achieved, corresponding to the theoretical predictions. Owing to the large wavelength range and the accurate complex field reconstruction, this resolution is, to the best of our knowledge, the best that has ever been achieved with multiple wavelength tomography. Note that it still can be improved by taking holograms in a larger wavelength range, which will reduce the central peak width of the filter function.

The proposed technique has the advantage of a simple and robust setup; all sensitive parts such as phase compensations or aberration corrections are

numerically controlled. The digital focusing capability of DHM also leads to an extended depth of field while keeping a relatively large NA to preserve high lateral resolution. This last point is a great advantage over equivalent optical coherence tomography techniques. The numerical possibilities of tomography by multiple wavelengths in digital holography open large signal processing possibilities to further enhance the tomographic results, as will be pointed out in a future paper.

This work was funded through research grants 2153-067068.01 and 205320-103885/1 from the Swiss National Science Foundation.

References

1. E. Wolf, "Three-dimensional structure determination of semi-transparent object from holographic data," *Opt. Commun.* **1**, 153–156 (1969).
2. W. H. Carter, "Computational reconstruction of scattering objects from holograms," *J. Opt. Soc. Am.* **60**, 306–314 (1970).
3. R. Dändliker and D. Weiss, "Reconstruction of three-dimensional refractive index from scattered waves," *Opt. Commun.* **1**, 323–328 (1970).
4. A. F. Fercher, H. Bartelt, H. Becker, and E. Wiltschko, "Image formation by inversion of scattered field data: experiments and computational simulation," *Appl. Opt.* **18**, 2427–2439 (1979).
5. V. Lauer, "New approach to optical diffraction tomography yielding a vector equation of diffraction tomography and a novel tomographic microscope," *J. Microsc.* **205**, 165–176 (2002).
6. A. Barty, K. A. Nugent, A. Roberts, and D. Paganin, "Quantitative phase tomography," *Opt. Commun.* **175**, 329–336 (2000).
7. F. Charrière, A. Marian, F. Montfort, J. Kühn, T. Colomb, E. Cuche, P. Marquet, and C. Depeursinge, "Cell refractive index tomography by digital holographic microscopy," *Opt. Lett.* **31**, 178–180 (2006).
8. J. C. Marron and K. S. Schroeder, "Holographic laser radar," *Opt. Lett.* **18**, 385–387 (1993).
9. J. C. Marron and K. W. Gleichman, "Three-dimensional imaging using a tunable laser source," *Opt. Eng.* **39**, 47–51 (2000).
10. E. Arons and D. Dilworth, "Analysis of Fourier synthesis holography for imaging through scattering materials," *Appl. Opt.* **34**, 1841–1847 (1995).
11. M. K. Kim, "Wavelength-scanning digital interference holography for optical section imaging," *Opt. Lett.* **24**, 1693–1695 (1999).
12. M. K. Kim, "Tomographic three-dimensional imaging of a biological specimen using wavelength-scanning digital interference holography," *Opt. Express* **7**, 305–310 (2000).
13. L. Yu and M. K. Kim, "Wavelength scanning digital interference holography for variable tomographic scanning," *Opt. Express* **13**, 5621–5627 (2005).
14. L. Yu and M. K. Kim, "Variable tomographic scanning with wavelength scanning digital interference holography," *Opt. Commun.* **260**, 462–468 (2006).
15. A. Dakoff, J. Gass, and M. K. Kim, "Microscopic three-dimensional imaging by digital interference holography," *J. Electron. Imaging* **12**, 643–647 (2003).
16. E. Cuche, F. Bevilacqua, and C. Depeursinge, "Digital holography for quantitative phase-contrast imaging," *Opt. Lett.* **24**, 291–293 (1999).
17. E. Cuche, P. Marquet, and C. Depeursinge, "Simultaneous amplitude-contrast and quantitative phase-contrast microscopy by numerical reconstruction of Fresnel off-axis holograms," *Appl. Opt.* **38**, 6994–7001 (1999).

18. T. Colomb, E. CuChe, F. Charrière, J. Kühn, N. Aspert, F. Montfort, P. Marquet, and C. Depeursinge, "Automatic procedure for aberration compensation in digital holographic microscopy and applications to specimen shape compensation," *Appl. Opt.* **45**, 851–863 (2006).
19. T. Colomb, J. Kühn, F. Charrière, C. Depeursinge, P. Marquet, and N. Aspert, "Total aberrations compensation in digital holographic microscopy with a reference conjugated hologram," *Opt. Express* **14**, 4300–4306 (2006).
20. T. Colomb, F. Montfort, J. Kühn, N. Aspert, E. CuChe, A. Marian, F. Charrière, S. Bourquin, P. Marquet, and C. Depeursinge, "Numerical parametric lens for shifting, magnification, and complete aberration compensation in digital holographic microscopy," *J. Opt. Soc. Am. A* **23** (2006).
21. P. Ferraro, S. D. Nicola, G. Coppola, A. Finizio, D. Alfieri, and G. Pierattini, "Controlling image size as a function of distance and wavelength in Fresnel-transform reconstruction of digital holograms," *Opt. Lett.* **29**, 854–856 (2004).
22. E. CuChe, P. Marquet, and C. Depeursinge, "Spatial filtering for zero-order and twin-image elimination in digital off-axis holography," *Appl. Opt.* **39**, 4070–4075 (2000).
23. F. Montfort, F. Charrière, T. Colomb, E. CuChe, P. Marquet, and C. Depeursinge, "Purely numerical correction of the microscope objective induced curvature in digital holographic microscopy," *J. Opt. Soc. Am. A* **23**, 2944–2953 (2006).
24. M. K. Kim, L. Yu, and C. J. Mann, "Interference techniques in digital holography," *J. Opt. A, Pure Appl. Opt.* **8**, S518–S523 (2006).